

Supporting information

Catalyst Characterization techniques

Powder X-ray diffraction (XRD) pattern of the calcined Ni/MCM-41 was recorded on a Rigaku-RAD-X system using monochromatized Cu K α radiation ($\lambda = 1.542\text{\AA}$). In general, the diffraction data were collected using continuous scan mode with a scan speed of 2 deg/min over the scan range of $2\theta = 1.5\text{--}15^\circ$ for low angle and for wide-angle ($2\theta = 30\text{--}70^\circ$) measurements. Transmission electron microscopy (TEM) images of the calcined Ni/MCM-41 was recorded on Philips Technai operating at 200 Kv. The powder was suspended in ethanol by ultrasonic method. A drop of this solution is placed on a grid with a holey carbon copper film and then allowed to dry, covered by a watch glass. N₂-adsorption measurements were carried out using a micromeritics ASAP 2400 analyzer. The volume of adsorbed N₂ was normalized to standard temperature and pressure. Before the experiment, samples were degassed at 300 °C for overnight. The specific surface area was determined from the linear part of the BET plot ($P/P_0 = 0.05\text{--}0.30$). The mesopore size distribution (PSD) was calculated using adsorption branch of the N₂ adsorption–desorption isotherm. For Fourier transformation infrared spectroscopy (FTIR), all the spectra were taken at room temperature on a Horiba spectrometer FT-720. Before measurement, samples were grounded with KBr and pressed into thin wafers. The UV-Vis spectra of the materials were recorded on a Shimadzu 2600 spectrophotometer operating in the reflection mode at a resolution of 2 nm using aluminum oxide as standard. XPS spectra were recorded on an Ulvac PHI 5601ci spectrometer. All the powder mineral samples were fixed onto a copper sample holder using double-sided sticky tape, which was then placed into a vacuum chamber attached with a turbo molecular pump. The samples were outgassed for 1 day under vacuum (10^{-5} Pa) and then introduced into the analysis chamber, where the pressure was kept around 1×10^{-7} Pa. To ensure the accuracy of the data, the

XPS system was calibrated using the peaks of Cu ($2P_{3/2}$) and Cu ($3P$) whose binding energies are 932.67 and 75.14 eV, respectively. The binding energy scales were adjusted to the highest C ($1s$) peak position equal to 284.8 eV. To calculate the chemical composition of the samples, empirical sensitivity factors were obtained from the relative area intensities of the photoelectron spectra of compounds of known chemical composition. Monochromatized Al $K\alpha$ X-ray (14 kV, 200 W) was used in place of a conventional X-ray source to obtain high-quality spectra to avoid overlapping of the satellite peaks; thus, uncertainty in the determinations of the peak position and peak area was nullified. An electron flood gun was used as a neutralizer, and the number of acquisitions was maintained at 12 for each analysis. For the used catalysts, additional cautions are taken to avoid the air exposure using glove box before subjected to XPS analysis.

Catalyst Characterization

Powder X-ray diffraction (XRD): A representative XRD pattern of calcined Ni/MCM-41 is shown in Figure S1a, which exhibits a typical low angle (1 0 0) reflection characteristics of mesoporous MCM-41¹ with the d_{100} spacings of 4.29 nm and hexagonal unit cell parameters a_0 ($2 d_{100} / \sqrt{3}$) = 4.95 nm. The high intensity of the (100) diffraction peak suggested the presence of hexagonal and ordered structure of Ni/MCM-41. Furthermore, the catalyst also maintained its mesoporous structure but d_{100} spacings was decreased to 3.84 nm (Figure S1b) after the reaction. Additional wide angle ($2\theta = 30^\circ$ to 90°) XRD peaks are appeared at $2\theta = 37.3, 43.2, 62.8, 75.4$ and 79.8 corresponds to NiO.² as displayed in Figure S1 as inset. There was no significant change in the higher angle spectra of the spent catalyst. No peak corresponding to Ni⁰ was detected.

Transmission Electron Microscopy (TEM): Figure S2 exhibited the TEM image of calcined Ni/MCM-41. TEM of the calcined sample shows a regular hexagonal array of uniform channels

which is characteristic of MCM-41 and confirms the occurrence of well-ordered hexagonal structure, and entirely consistent with the XRD results, however, no NiO particles were detected due to the low Ni content.

N₂ adsorption desorption: Porosity assessments of the material has been achieved from the investigations on N₂ adsorption-desorption isotherms (Figure S3). Calcined Ni/MCM-41 showed a type IV isotherm according to the IUPAC classification³, typical of conventional mesoporous materials like MCM-41⁴. It exhibits a sharp increase at $P/P_0 < 0.1$ and $P/P_0 \sim 0.34$ as shown in Figure S4. The inflection position at $P/P_0 = 0.2-0.3$ was due to the presence of primary mesopores while the second increase at $P/P_0 > 0.45$ arises from capillary condensation with multi-layers adsorption on the inner surface.⁵ The BET (Brunauer, Emmett and Teller) surface area was 972 m²g⁻¹ and the average pore diameter obtained was ~ 3.2 nm from the pore size distribution (Figure S4; inset). Note that according to IUPAC recommendations, pores are classified as micropores (< 2 nm), mesopores (width between 2 and 50 nm), and macropores (> 50 nm).

Fourier transformation infrared spectroscopy (FTIR): The FTIR spectra of fresh and used catalysts were recorded in the range of 4000- 400 cm⁻¹ at room temperature and depicted in Figure S4a and S4b respectively. Figure S4a shows a typical FTIR spectra of MCM-41 consisting of the absorption peaks at 1051 cm⁻¹, 806 cm⁻¹ assigned to the asymmetric and symmetric stretch of the Si-O-Si bridges, respectively. Moreover, the peak at 456 cm⁻¹ were due to Si-O bending vibration,⁶ whereas, those peaks are unidentifiable in the spectra of spent catalyst (Figure S4b) due to the presence of Al₂O₃.⁷ Furthermore, both of the spectra show a broad peak around ~ 3430 cm⁻¹ and ~ 1635 cm⁻¹ assigned to H-O-H stretching and -OH bending vibration of water, respectively. ⁸
⁹ Typical adsorption band corresponds to the adsorption of atmospheric CO₂ was located at 2373-2343 cm⁻¹.¹⁰ Instead of the characteristic band of acetaldehyde at 2723 and 1730 cm⁻¹, FTIR spectra

of the spent catalyst shows three new peaks at 1627 cm^{-1} , 1577 cm^{-1} and 1467 cm^{-1} , which assigned to CO enolic band,¹¹ $\nu_{\text{as}}\text{ COO}^-$ group¹² and $\nu_{\text{s}}\text{ CO}_3$ (mono- or bidentate) respectively occurs through the reaction between surface hydroxyl group and CO_2 .¹³

UV-vis spectroscopy: UV-vis spectroscopy is well suited to characterize the nature and coordination structure of various transition metal ions. Figure S5 shows the UV-vis spectra of Ni/MCM-41, to demonstrate the coordination of Ni in silica framework. Notably, parent MCM-41 exhibits no detectable absorption in the UV or visible region (not shown), hence, absorption bands detected in the spectra corresponds to Ni in different coordination state. The calcined material displayed a peak at 210 nm related to the charge transfer from O^{2-} to Ni^{2+} . In addition, a broad peak at 245 nm along with several small peaks in the region of 350-450 nm and 450-750 nm, were also visible, which suggested the presence of NiO and corresponded well with the results of XRD. Assignment of the absorption bands at 367 nm and 395 nm were attributed to the spin-allowed transitions of Ni^{2+} in an octahedral coordination (${}^3\text{A}_{2\text{g}} \rightarrow {}^3\text{T}_{1\text{g}}(\text{P})$, ${}^3\text{A}_{2\text{g}} \rightarrow {}^3\text{T}_{1\text{g}}(\text{F})$).¹⁴ In addition, a large and weak band around 609 nm, which tentatively assigned to Ni^{2+} in a tetrahedral environment was also discerned.¹⁵

X-ray photo electron spectroscopy (XPS): Beside UV-visible spectra, XPS was employed to understand the chemical state of Ni as well as change in the metal environment before and after the reaction. Fresh and spent catalysts were investigated using XPS and the results are shown in Figure S6. Figure S6a and S6b exhibited the 2p region spectra of Ni in fresh and spent catalysts, respectively. The Ni $2\text{p}_{3/2}$ spectra of the fresh catalyst contain a charge transfer peak centered at 854.2 eV with a shoulder and a satellite peak, which were attributed to the presence of NiO¹⁶ and agree well with the experimental results of XRD and UV-vis spectroscopic analysis. Moreover, the Ni $2\text{p}_{1/2}$ peak observed in the spectra of fresh catalyst at 872 eV also provides further evidence

of the presence of NiO. Regarding the interpretation of Ni 2p spectra, satellites and number of shake up peaks are originated in higher level of binding energy of the Ni 2p_{3/2} and Ni 2p_{1/2} region due to mixing of d-d transition and enhancement of Ni 3d→O2p hybridization.¹⁶ There was no significant change observed in the spectra of used catalyst but Ni 2p_{3/2} peak was slightly shifted to 853.5 eV. There was no peak related to Ni⁰ species detected in the higher binding energy region. (Figure S6b), which corresponded well with the results of XRD analysis.

Analytical method for product identification

After the reaction, the liquid product mixture was separated from the solid catalyst by filtration. All products were first identified by GC-MS (Varian CP3800) against a standard, which was also used for qualitative analysis. Quantification of the products was obtained by a multi-point calibration curve for each product. Quantitative analysis was carried out using a GC (HP 6890) equipped with Innowax capillary column (Agilent, 30 m x 0.32 mm, 0.25 μm) and a flame ionization detector. The GC method used was as follows: An initial oven temperature of 40 °C was held for 5 minutes. In the next step, the temperature was ramped at 10 °C/min. until it reached 240 °C and held for 20 minutes followed by the increase in temperature to 230 °C ramped at 7.5 °C/min. and held for 20 minutes. Due to the technical difficulties, calculation of carbon balance⁵ including gaseous product was difficult (large volume of CO₂ was in the system), however, considering the liquid product ~ 96.1 % carbon balance can be obtained.

The selectivity to each product was calculated by the following expression

$$S_i = C_i / \sum C_p,$$

where C_i is the concentration of the product 'i' and $\sum C_p$ is the total concentration of the product.

TOF= number of moles reacted/ moles of metal x time

Lactic acid productivity= moles of lactic acid obtained /catalyst used (g) x time

Computational methodology

All the reaction energy calculations were performed by density functional theory (DFT)¹⁷ using DMol³^{18, 19} of DASSAULT SYSTEMES BIOVIA. Gradient corrected functional BLYP^{20, 21} and the DNP basis set²² with the spin unrestricted option were used throughout the calculations. The initial spin states were decided according to the spin states of the metal cations present in the model. The Kohn–Sham equation was expanded in a double numeric quality basis set with polarization functions (DNP). The orbital cutoff range and Fermi smearing were selected as 5.0 Å and 0.001 Ha, respectively. The self-consistent-field (SCF) procedures were performed to obtain well-converged geometrical and electronic structures at a convergence criterion of 10^{−6} a. u. The energy, maximum force, and maximum displacement convergence were set to 10^{−6} Ha, 0.002 Ha Å^{−1}, and 0.005 Å, respectively. The activation energy was calculated using the transition state search algorithm as implemented in DMol³ with the nudged elastic band method (NEB). All the calculations were performed using the Conductor-like Screening Model (COSMO)^{23, 24} to consider the effect of solvation. We have used 78.54 as the dielectric constant for water.

Figure S1: XRD pattern of Ni/MCM-41 (a) before and (b) after reaction. Inset shows wide angle pattern corresponding to Ni in the oxide form.

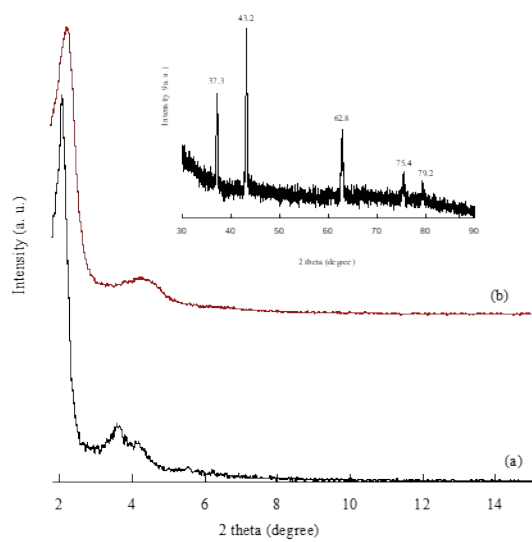


Figure S2: TEM image of calcined Ni/MCM-41 shows ordered structure.

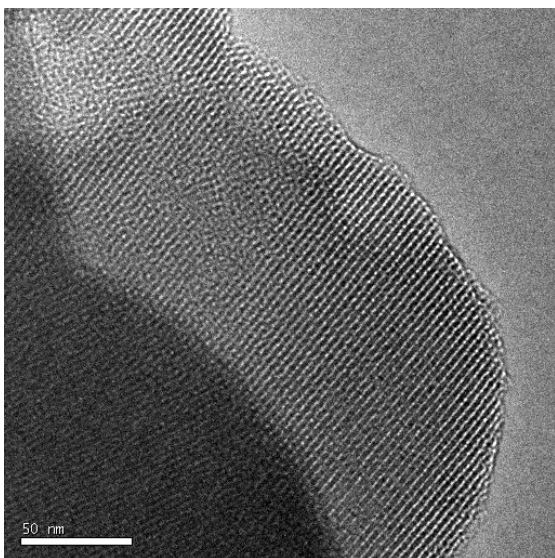


Figure S3: N₂ adsorption-desorption isotherm of calcined Ni/MCM-41. Inset shows BJH (Barrett-Joyner-Halenda) pore size distribution obtained from the adsorption branch.

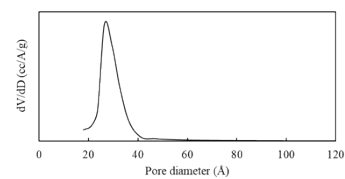
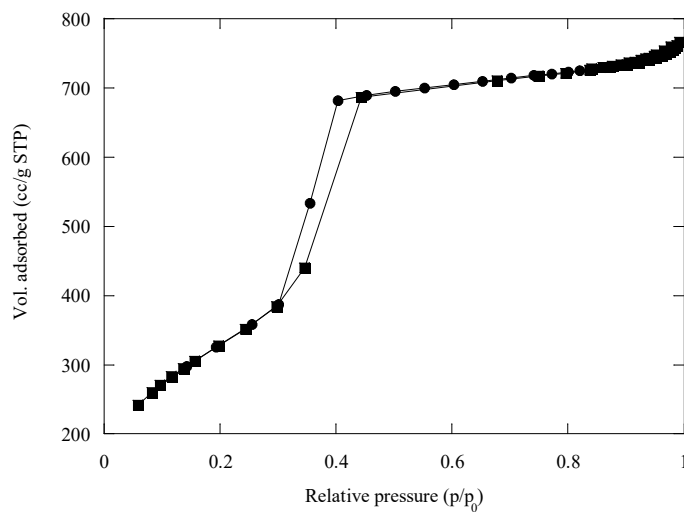


Figure S4: FTIR spectra of catalyst (a) before and (b) after the transformation of acetaldehyde to lactic acid.

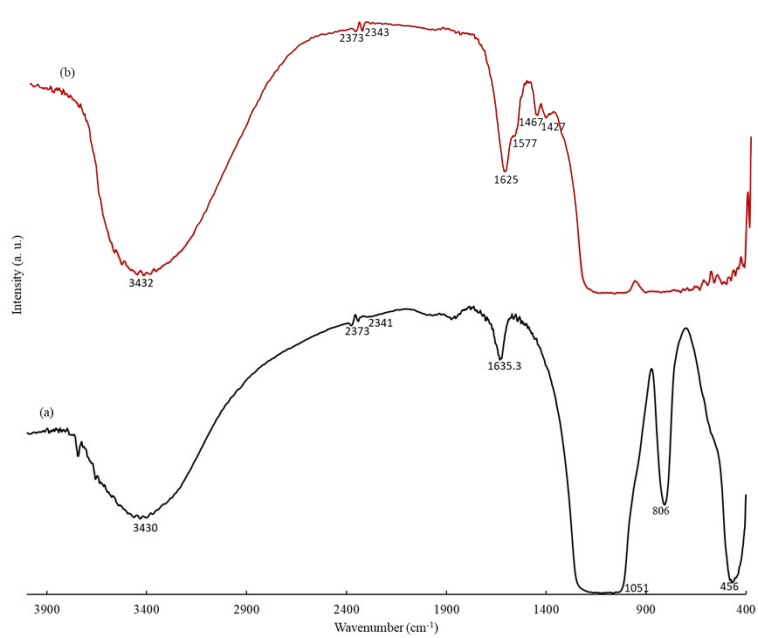


Figure S5: UV-vis spectra of Ni/MCM-41 catalyst taken at room temperature.

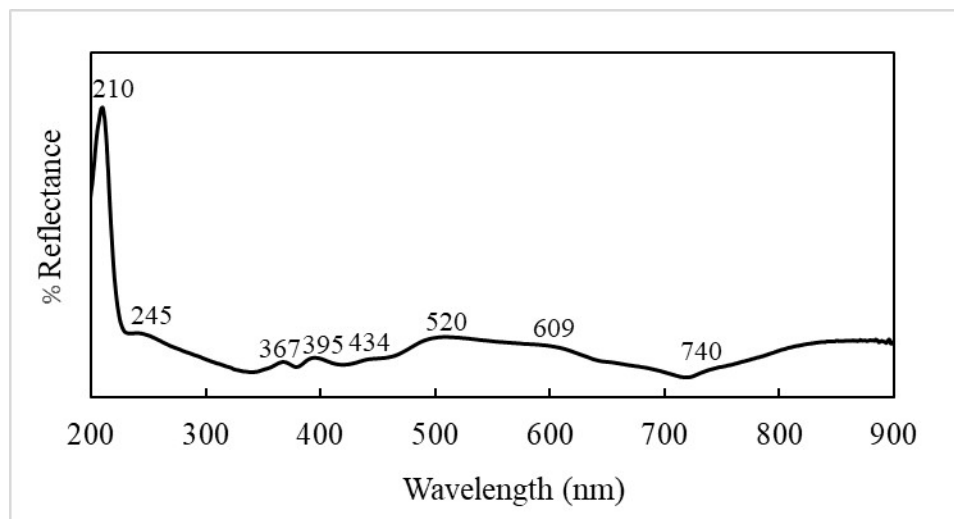


Figure S6: XPS of Ni/MCM-41 (a) before and (b) after the conversion of acetaldehyde to lactic acid.

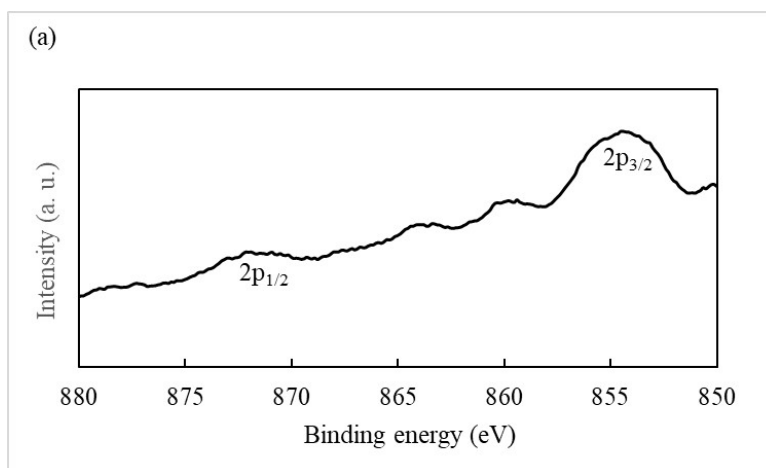
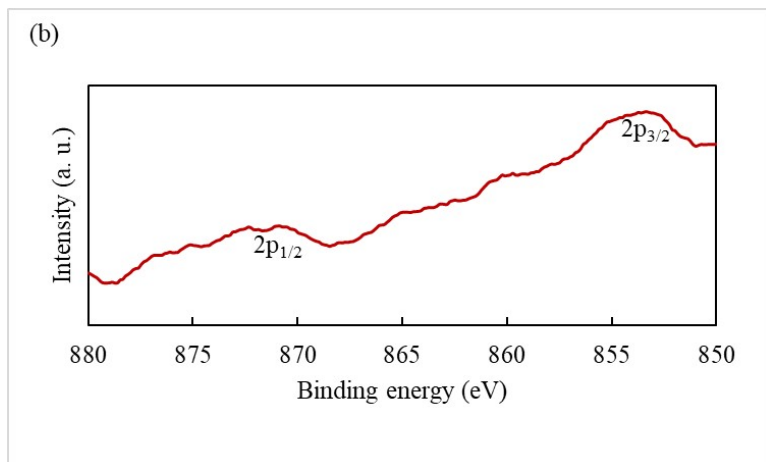


Figure S7: ^1H NMR spectra of lactic acid in the product mixture.

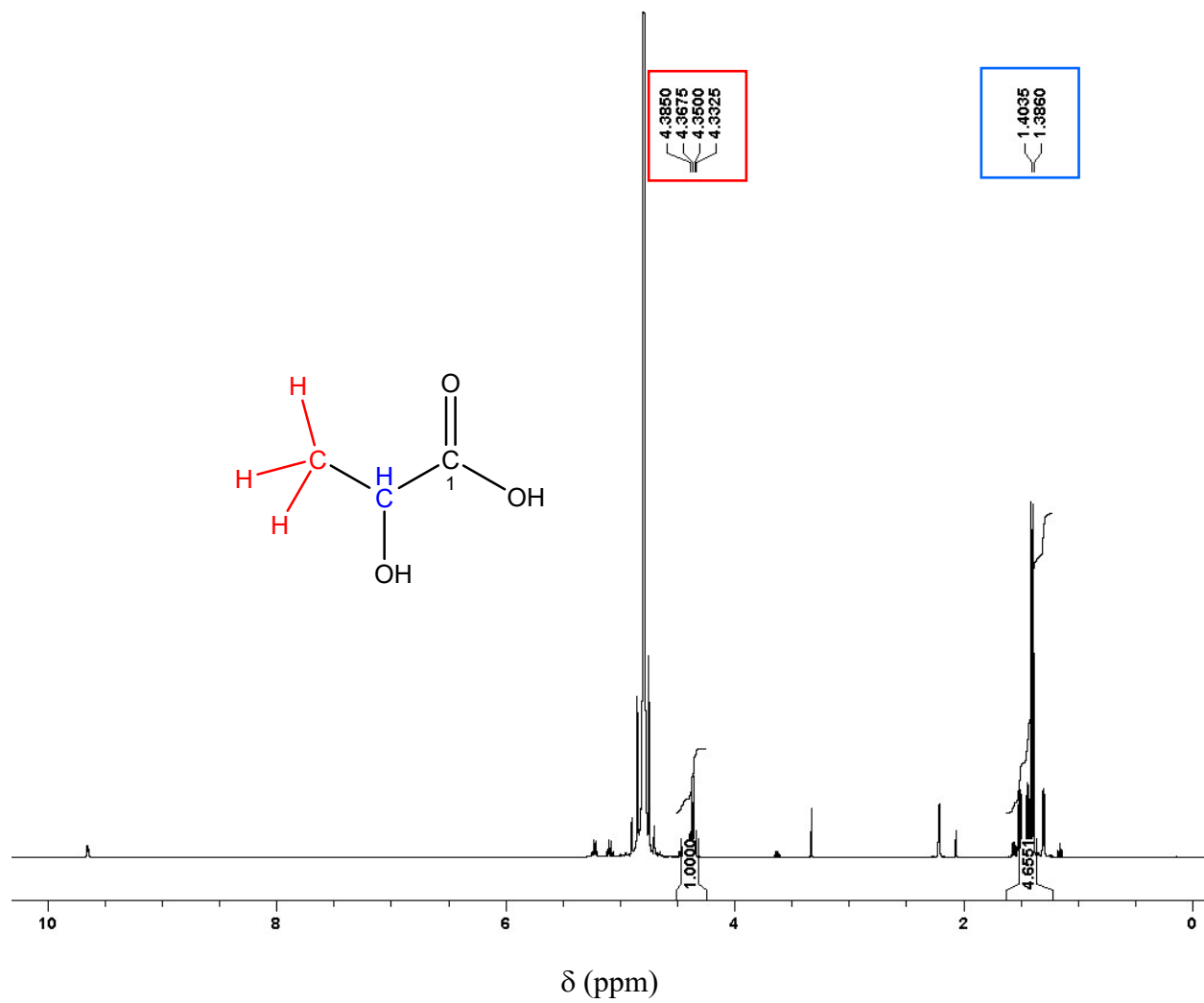


Figure S8: Variation of turnover frequency (TOF) with (a) CO₂ pressure, (b) temperature, (c) volume of water and (d) amount of Al₂O₃.

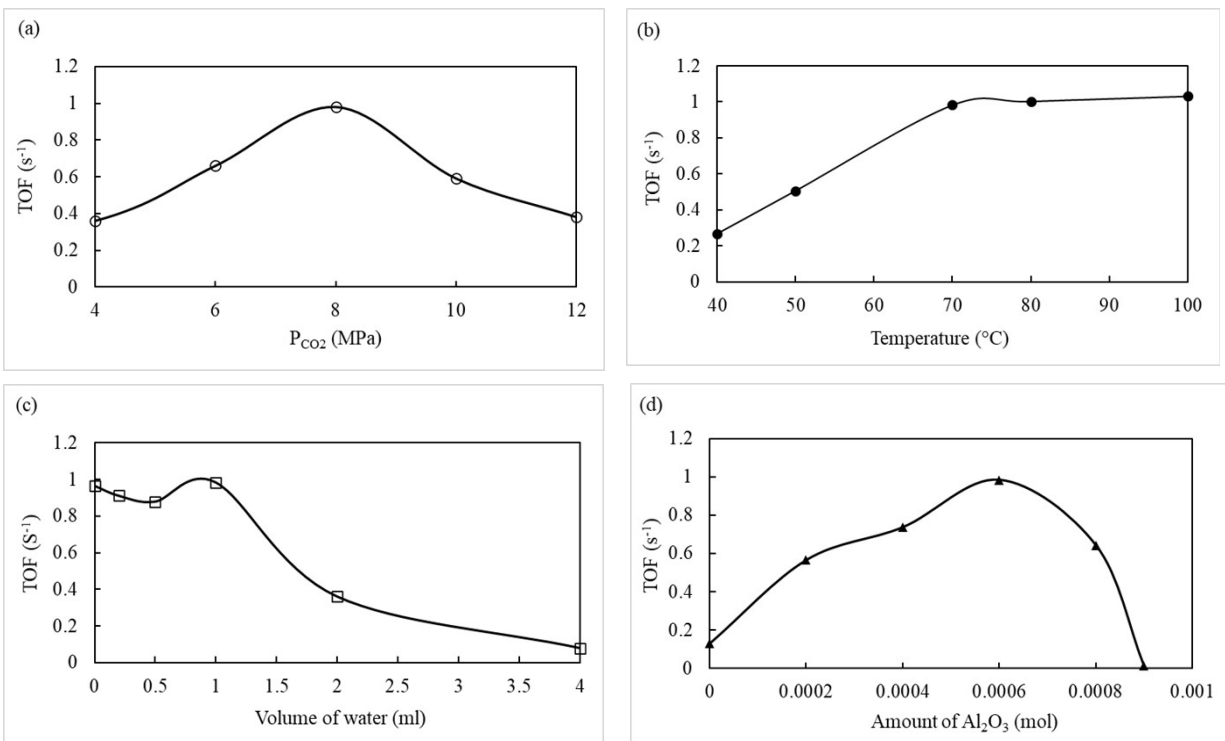


Figure S9: Phase observation of CO₂-H₂-acetaldehyde (a) empty cell, (b) 4 MPa, (b) 8 MPa and (c) 12 MPa of CO₂ pressure. For better understandings water and solid catalyst were omitted.

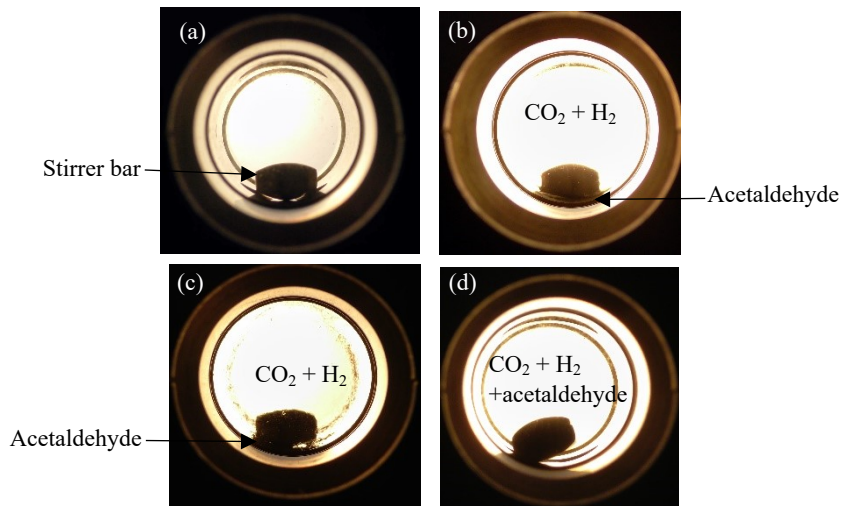


Figure S10: Energy profile of the total catalytic cycle of Ni catalyzed conversion of acetaldehyde to lactic acid.

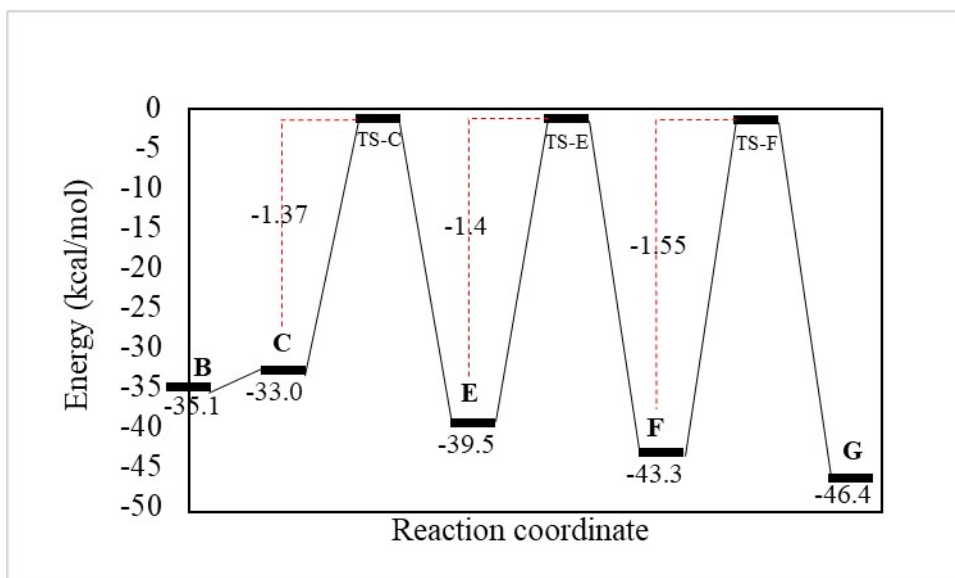
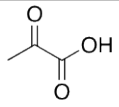
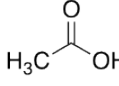

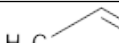
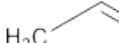
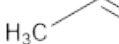


Table S1: Control experiments with different substrates

Entry	Substrate	Yield of lactic acid (%)
1	 Pyruvic acid	3.5
2	 Acetic acid	0
3	CO	0
4 ^a	 Acetaldehyde	0.6
5 ^b	 Acetaldehyde	2.8
6	 Acetaldehyde	0 ^c , 0 ^d , 0.12 ^e , 0.5 ^f , 3.43 ^g
7 ^h	 Acetaldehyde	0

Reaction conditions: catalyst=0.02g, substrate=0.1 g, water= 1ml, temperature=70 °C, P_{CO_2} = 1 MPa, P_{H_2} = 1 MPa and reaction time=3h; ^aHCOOH (0.1 mmol); ^bK₂CO₃ (0.2 mmol). For Entry 4 and 5 no CO₂ was added. For entry 6

^c without CO₂, ^d without water, ^e without hydrogen, ^f without Ni catalyst and ^g without Al₂O₃.

^h reduced Ni/MCM-41

References

1. J. S. Beck, J. C. Vartuli, J. W. Roth, M. E. Leonowicz, C. T. Kresge, K. D. Schmitt, C. T. W. Chu, D. H. Olsen, E. W. Sheppard, S. C. McCullen, J. B. Higgins, J. L. Schlenker, *J. Am. Chem. Soc.* **1992**, *114*, 10834-10843.
2. J. T. Richardson, R. S. Martyn, V. Twigg, *Appl. Catal. A: General* **2003**, *246*, 137-150.
3. S. J. Gregg, K. S. W. Sing, Adsorption, Surface Area and Porosity, Academic Press, New York, 1982.
4. D. Y. Zhao, J. Feng, Q. Huo, N. Melosh, G. H. Fredrickson, B. F. Chmelka, G. D. Stucky, *Science* **1998**, *279*, 548-552.
5. D. Y. Zhao, Q. S. Huo, J. L. Feng, B. F. Chmelka, G. D. Stucky, *J. Am. Chem. Soc.* **1998**, *120*, 6024-6036.
6. Y. Shu, Y. Shao, X. Wei, X. Wang, Q. Sun, Q. Zhang and L. Li, *Microporous Mesoporous Mater.* **2015**, *214*, 88-94.
7. T. Z. Ren, Z. Y. Yuan, B. L. Su, *Langmuir* **2004**, *20*, 1531-1534.
8. A. C. Tas, P. J. Majewski, F. Aldinger, *J. Am. Ceram. Soc.* **2002**, *85*, 1421-1429.
9. G. Li, C. Peng, C. Li, P. Yang, Z. Hou, Y. Fan, Z. Cheng and J. Lin, *Inorg. Chem.* **2010**, *49*, 1449-1457.
10. K. L. Kauffman, J. T. Culp, A. Goodman, C. Matranga, *J. Phys. Chem. C* **2011**, *115*, 1857-1866.
11. G. W. Mines and Harold Thompson, *Proc. R. Soc. Lond. A.* **1975**, *342*, 327-339.
12. W. R. Heinz, T. Kratky, M. Drees, A. Wimmer, O. Tomanec, S. Günther, M. Schuster, R. A. Fischer, *Dalton Trans.* **2019**, *48*, 12031-12039.
13. M. E. Rudbeck, S. Kumar, M.-A. Mroginski, S. O. N. Lill, M. R. A. Blomberg, and A. Barth, *J. Phys. Chem. A* **2009**, *113*, 2935-2942.
14. M. Tanaka, A. Itadani, Y. Kuroda, and M. Iwamoto, *J. Phys. Chem. C* **2012**, *16*, 5664-5672.
15. B. Scheffer, J. J. Heijeinga, and J. A. Moulijn, *J. Phys. Chem.* **1987**, *91*, 4752-4759.
16. A. P. Grosvenora, M. C. Biesinger, R. St. C. Smart, N. S. McIntyre, *Surf. Sci.*, **2006**, *600*, 1771-1779.
17. W. Kohn, L. Sham, *J. Phys. Rev. A* **1965**, *140*, 1133-1137.
18. B. Delley, *J. Chem. Phys.* **1990**, *92*, 508-517.

19. B. Delley, *J. Chem. Phys.* **2000**, *113*, 7756–7764.
20. A. Becke, *J. Chem. Phys.* **1988**, *88*, 2547-2553.
21. C. Lee, W. Yang, R. G. Parr, *Phys. Rev. B* **1988**, *37*, 785-789.
22. B. Delley, *Phys. Rev. B* **2002**, *66*, 155125-155134.
23. A. Klamt, G. Schrumann, *J. Chem. Soc. Perkin. Trans.* **1993**, *2*, 799-805.
24. B. Delley, *Mol. Simul.* **2006**, *32*, 117-123.